

www.acsami.org Research Article

Growth Conditions and Interfacial Misfit Array in SnTe (111) Films Grown on InP (111)A Substrates by Molecular Beam Epitaxy

Qihua Zhang,* Maria Hilse, Wesley Auker, Jennifer Gray, and Stephanie Law*



Cite This: ACS Appl. Mater. Interfaces 2024, 16, 48598-48606



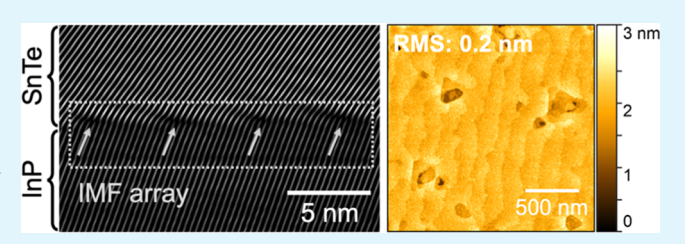
ACCESS I

Metrics & More

Article Recommendations

Supporting Information

ABSTRACT: Tin telluride (SnTe) is an IV-VI semiconductor with a topological crystalline insulator band structure, high thermoelectric performance, and in-plane ferroelectricity. Despite its many applications, there has been little work focused on understanding the growth mechanisms of SnTe thin films. In this manuscript, we investigate the molecular beam epitaxy synthesis of SnTe (111) thin films on InP (111)A substrates. We explore the effect of substrate temperature, Te/Sn flux ratio, and growth rate



on the film quality. Using a substrate temperature of 340 °C, a Te/Sn flux ratio of 3, and a growth rate of 0.48 Å/s, fully coalesced and single crystalline SnTe (111) epitaxial layers with X-ray rocking curve full-width-at-half-maxima of 0.09° and root-mean-square surface roughness as low as 0.2 nm have been obtained. Despite the 7.5% lattice mismatch between the SnTe (111) film and the InP (111)A substrate, reciprocal space mapping indicates that the 15 nm SnTe layer is fully relaxed. We show that a periodic interfacial misfit (IMF) dislocation array forms at the SnTe/InP heterointerface, where each IMF dislocation is separated by 14 InP lattice sites/13 SnTe lattice sites, providing rapid strain relaxation and yielding the high quality SnTe layer. This is the first report of an IMF array forming in a rock-salt on zinc-blende material system and at an IV-VI on III-V heterointerface, and highlights the potential for SnTe as a buffer layer for epitaxial telluride film growth. This work represents an important milestone in enabling the heterointegration between IV-VI and III-V semiconductors to create multifunctional devices.

KEYWORDS: chalcogenide, interfacial misfit array, IV-VI semiconductor, III-V semiconductor, molecular beam epitaxy, wafer-scale synthesis, thin film

1. INTRODUCTION

Tin telluride (SnTe) is a narrow bandgap semiconductor with many desirable properties: it has a high thermoelectric figure of merit with nontoxic components, 1-7 it is a topological crystalline insulator, 8-14 and it exhibits ferroelectric behavior when its crystal structure undergoes a phase transition. 15-19 Bulk SnTe crystals have a structural phase transition (from rock-salt crystal to rhombohedral) temperature (T_C) of ~100 K_{c}^{15} but T_{c} can be greatly enhanced when the thickness of a SnTe thin film is reduced. SnTe films with a thickness of 1 unit cell (6.32 Å) have shown a T_c of 270 K. The discovery of near-room-temperature $T_{\rm C}$ makes SnTe thin films feasible for a wide range of ferroelectric applications including nonvolatile memory devices and nonlinear optoelectronics. 18,20,24-26 In addition, the band structure of SnTe is topologically nontrivial. Theoretical calculations predict that gapless surface states can be observed on both the (001) and (111) planes of SnTe, due to the mirror symmetry of its rock-salt crystal structure.^{8,10} Tanaka et al. and Zhang et al. were among the first to experimentally confirm the Dirac-cone-like band structure on SnTe (100) and (111) using angle-resolved photoemission spectroscopy measurements. 9,13

In addition to its attractive material properties, SnTe also serves as an important buffer layer for Te-based heterostructures. For example, SnTe is a popular back surface field layer for photovoltaic devices due to its narrow bandgap and high hole concentration, and is thus often used as a buffer layer for CdTe-based solar cell heterostructures. ^{27–29} SnTe can also be used as a spacer material for antiferromagnetic EuTe quantum dots, due to the relatively low lattice mismatch between the two alloys. 30,31 Very recently, with a thin (2 nm) SnTe buffer layer, (Sn-Pb-In)Te alloys exhibited superconductivity and semimetal behavior with electron mobilities exceeding 5000 cm $^{2}/(V s)$. 32,33

The quality of SnTe strongly affects its intrinsic properties as well as the performance of devices incorporating SnTe, so it is critical to understand the growth mechanism of SnTe using a mature synthesis technique. Molecular beam epitaxy (MBE) is a promising technique for the synthesis of high-quality SnTe layers due to its ultrahigh vacuum (UHV) growth environment, use of high purity source materials, and in situ surface

Received: June 21, 2024 Revised: August 15, 2024 Accepted: August 16, 2024 Published: August 28, 2024





monitoring capabilities. In the past, growths of SnTe films by MBE have been reported by multiple research groups.³³ However, few of the efforts have been focused on understanding the growth mechanisms of SnTe films. Masuko et al. demonstrated the growth of $Sn_xIn_{1-x}Te$ (111) thin films with a full-width-at-half-maximum (fwhm) of 0.11° in X-ray diffraction (XRD) rocking curves, yet no analysis of surface morphology was provided.³³ Recently, the research group led by Kobayashi studied the surface morphology and electronic properties of SnTe (100) layers. 34,35 However, these films also contained misoriented (111)-SnTe domains. A thorough investigation of how growth conditions impact the quality of SnTe thin films is thus needed.

In addition, to fully realize the potential of SnTe buffer layers, developing a technique for synthesizing ultrathin relaxed layers with a low density of threading dislocations on a latticemismatched substrate is crucial. Interfacial misfit (IMF) arrays are a longstanding method for obtaining high-quality relaxed epilayers on heterogeneous substrates. IMF arrays consist of misfit dislocations that are uniformly spaced at the epilayer/ substrate heterointerface and which provide rapid and effective strain relaxation (>99%) at the interface, thus creating a fully relaxed epilayer with low film thickness. In the past, IMF arrays have only been observed in III–V semiconductor epilayers.^{38–44} A well-established example is the GaSb epilayer on a GaAs substrate: despite their 7.8% lattice mismatch, the threading dislocation density of GaSb on GaAs is on the order of 10⁸ cm⁻² with the use of an IMF array. 44 Similarly, with the use of an IMF array, AlSb epilayers can be grown with almost full strain relaxation on Si (100) substrates, which has a 13% lattice-mismatch to the epilayer. 39 Although there has recently been one report of an IMF array in a (111)-oriented system, 44 there is no report of IMF arrays in a (111)-oriented IV-VI epilayer on a (111)-oriented III-V substrate. It is worth mentioning that very recently, Jung et al. reported the growths of PbTe on InP using an island reorientation process, where various types of misfit dislocations were formed at the heterointerface, leading to formations of single crystalline PbTe (111) films on InP (111) substrates.⁴⁵

In this work, we use the IMF array technique for the growth of high quality SnTe epitaxial layers on InP (111)A substrates, which are chosen for their low cost and large-scale availability. The substrate has a 7.5% lattice mismatch to SnTe, 46 similar to that in the GaSb/GaAs material system. A downside of using an InP (111)A substrates is the difference in the crystal structure between SnTe (rock-salt) and InP (zinc-blende). Despite these differences, we identify an optimized growth window comprising a substrate temperature in the range of 300–340 °C, a Te/Sn flux ratio of \sim 3, and growth rate of 0.48 Å/s, which yields fully coalesced, single crystal, relaxed SnTe (111) films with a fwhm less than 0.1° in the SnTe (222) XRD rocking curve and a root-mean-square (RMS) film surface roughness as low as 0.2 nm in atomic force microscopy (AFM). From scanning transmission electron microscopy (STEM) analysis at the SnTe/InP heterointerface, we find an IMF dislocation array, where each misfit dislocation is separated evenly by 14 InP lattice sites and 13 SnTe lattice sites, which relieves the strain and yields the high quality SnTe epilayer. This result marks the first demonstration of an IMF array in the rock-salt/zinc-blende system, as well as the integration of IV-VI films on III-V semiconductors.

2. EXPERIMENTAL DETAILS

As-received 2-in. undoped InP (111)A wafers (WaferTech) were first diced into 1×1 cm² pieces. The diced substrate was then submerged sequentially in acetone and isopropyl alcohol in an ultrasonic bath to remove surface contamination, followed by a deionized water rinse at room temperature. The substrate was further subjected to a UVozone treatment for 5 min to degrade organic contaminants. After the cleaning process, the substrate was immediately transferred to the load lock chamber with a base pressure of 5×10^{-9} Torr and outgassed at 200 °C for 2 h before being loaded into the MBE chamber. Prior to growth, the substrate was thermally annealed in the UHV chamber at 600 °C for 10 min to desorb the residual surface oxide. A tellurium flux in the range of $0.28-2.3 \times 10^{14} \text{ cm}^{-2}/\text{s}$ was supplied during the annealing process. A reflection high electron diffraction (RHEED) system with an electron beam energy of 15 keV (STAIB Instruments and kSA 400 analytical RHEED software) was used to monitor the surface of the substrate as well as the SnTe growth.

All SnTe growths were performed in a DCA Instruments R450 MBE system (instrument details at 10.60551/gqq8-yj90) with a base pressure of 5 \times 10⁻¹⁰ Torr. The Sn flux was supplied by thermal evaporation of high purity Sn (5 N) in a dual-filament effusion cell. The Te flux was supplied by evaporation of Te (5 N purity) in a lowtemperature effusion cell. Both fluxes were calibrated at room temperature using a ColnaTec quartz crystal microbalance operating at 6 MHz using tooling factors determined from physical film thickness measurements prior to SnTe growth. All SnTe layers were grown under Te-rich conditions to minimize Te re-evaporation and suppress metal droplet formation. For the current study, the maximum nominal growth rate of the SnTe film was 0.48 Å/s, where the operating temperature in the Sn effusion cell reached its maximum rated temperature. At the end of growth, all samples were annealed for 3 min in a Te environment at the growth temperature before being cooled to room temperature at a rate of 50 °C/min.

High resolution XRD measurements of the SnTe thin films were performed using a Malvern PANalytical 4-circle X'Pert³ system equipped with a hybrid 2-bounce asymmetric Ge(220) monochromator and PIXcel3D detector with an antiscatter slit. All XRD scans were taken at room temperature. The 2θ - ω scan was employed to determine the orientation of the as-grown SnTe films. Reciprocal space mapping (RSM) was performed on the SnTe film and the InP substrate on the (222) and (224) diffraction peaks, respectively. X-ray reflectivity (XRR) measurements were used to determine the thickness of the SnTe layers. For XRR, an X-ray mirror (Cu with a Si parabolic mirror and 1/32° divergence slit) was used as the beam incidence optics, along with a parallel plate beam collimator with 0.09 reflectivity slit as the diffracted beam optics. The thicknesses of the SnTe films (Sample A-G, excluding Sample E) were in the range of 12-15 nm. Figure S1 displays an exemplary XRR measurement and the fitting result of Sample G, which has a thickness of ~14.6 nm.

The surface morphology of SnTe layers was examined by a Bruker Dimension Icon atomic force microscope operating in peak force tapping mode with a SCANASYST-AIR probe, which has a nominal spring constant of 0.4 N/m. Scan parameters include a scan rate of 0.5 Hz, a lateral resolution of 512 pixels/line, and a peak force frequency of 2 kHz.

The as-grown SnTe film was prepared for cross-sectional STEM investigation using an FEI Helios Nanolab 660 dual-beam focused ion beam system. Carbon deposition was achieved using both electron beam and ion beam methods. Initially, electron beam-induced carbon deposition was conducted at 5 kV at 26 nA to create a protective layer on the sample surface. Subsequently, ion beam-induced carbon deposition was performed at 30 kV at 1 nA, enhancing the structural integrity of the deposited layer. For the final thinning and cleaning stages, the ion beam settings were adjusted to a lower energy of 2 kV, optimizing the precision of the milling process and minimizing potential damage from the ion beam. This combination of methodologies allowed for controlled sample manipulation, ensuring high-resolution imaging and analysis. A double aberration corrected FEI Titan3 G2 60-300 S/TEM system operating in STEM mode with a resolution of 0.07 nm was used for acquiring the STEM images of the as-prepared lamella. A high brightness electron source (X-FEG) operating at 300 kV and a high-angle annular dark field (HAADF) detector with a collection angle of 50-100 mrad was used for collecting HAADF-STEM images.

3. RESULTS AND DISCUSSION

3.1. Effect of Substrate Temperature Deduced by in Situ RHEED. We first studied the effect of substrate temperature (T_{sub}) on the growth of SnTe thin films using in situ RHEED monitoring. In this experiment, the growth rate was kept at 0.12 Å/s and the Te/Sn flux ratio was maintained at 2. Figure 1a shows the RHEED patterns of the InP (111)A

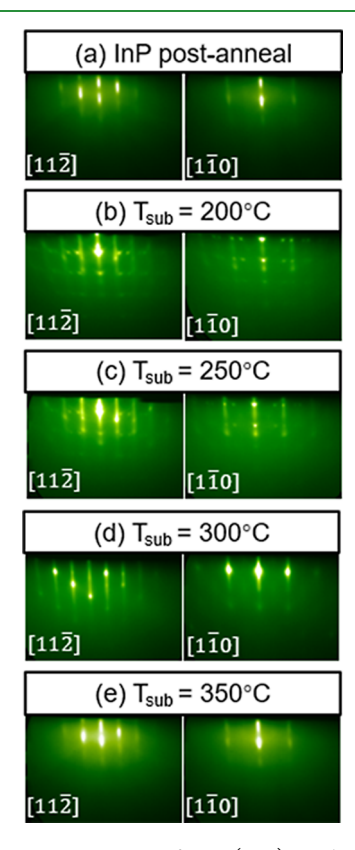


Figure 1. (a) RHEED pattern of InP (111)A substrate taken after annealing at 600 °C for 10 min in Te environment. (b-e) RHEED patterns taken immediately after the growths of SnTe layers with $T_{\rm sub}$ of (b) 200, (c) 250, (d) 300, and (e) 350 °C.

substrate along the $[11\overline{2}]$ and $[1\overline{10}]$ directions taken after thermal deoxidation. A typical bright, streaky pattern is observed, indicating a clean surface free of In droplets.⁴⁷ Figure 1b-e subsequently show the RHEED patterns taken immediately after the growth of the SnTe films at T_{sub} of 200, 250, 300, and 350 °C, respectively. At 200 °C, spotty patterns can be observed in both directions with hazy diffraction rods in the $[1\overline{10}]$ direction, indicating the formations of rough threedimensional (3D) islands on the substrate surface. The spacing between the two sets of spotty patterns is consistent with the pattern of the SnTe (001) surface, suggesting that the layer contains a mixture of (111)- and (001)-oriented SnTe domains. As the substrate temperature increases to 250 °C, more pronounced streaks can be observed along the $[11\overline{2}]$ direction, yet spots remain the dominant feature in the [110] direction. By further increasing the substrate temperature to

300 °C, bright and streaky patterns free of Laue ring and chevron are seen in both directions (Figure 1d), indicating the formation of a single-crystalline SnTe thin film with good inplane epitaxial alignment. Similar RHEED patterns were recorded for substrate temperatures up to 340 °C (not shown). However, at T_{sub} of 350 °C, solely RHEED patterns similar to the InP (111)A substrate were observed (Figure 1e), indicating that no film was deposited due to a high desorption and re-evaporation rate of surface adatoms and Sn-Te nuclei at this temperature. In summary, an optimal window of T_{sub} = 300-340 °C was identified through RHEED for SnTe film growth.

4. EFFECT OF TE/SN FLUX RATIO ON THE FILM SURFACE MORPHOLOGY

Within the optimal substrate temperature window (300–340 °C), the effect of the tellurium to tin (Te/Sn) flux ratio on the surface morphology of the SnTe film was further evaluated. Table 1 summarizes the growth conditions for a series of

Table 1. Growth Parameters of Samples a to D Including Sn Flux, Te Flux, Te/Sn Flux Ratio, Film Growth Rate^a

sample no.	Sn flux (cm^{-2}/s)	Te flux (cm ⁻² /s)	Te/Sn flux ratio	SnTe growth rate (Å/s)	RMS roughness (nm)
A	3.8×10^{13}	3.8×10^{13}	1	0.24	6.5
В	3.8×10^{13}	7.6×10^{13}	2	0.24	3.5
C	3.8×10^{13}	1.1×10^{14}	3	0.24	0.9
D	3.8×10^{13}	1.9×10^{14}	5	0.24	6.9

^aThe film surface RMS roughness calculated from a 2 × 2 μ m² AFM image for each sample is also listed.

samples in which the flux ratio was changed while the substrate temperature, growth rate, and film thickness were held constant at 340 $^{\circ}$ C, 0.24 Å/s, and \sim 15 nm, respectively. The surface morphology and in situ RHEED patterns of these samples are presented in Figure 2. By comparing the film

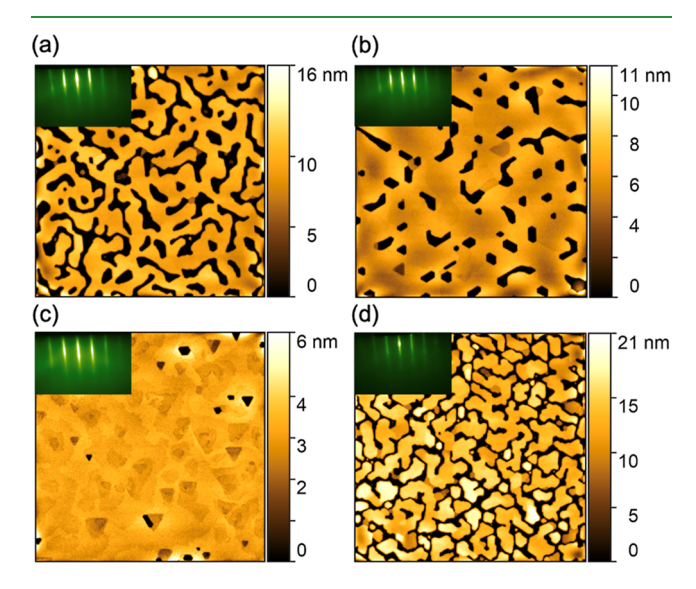


Figure 2. AFM images of SnTe films grown with a Te/Sn flux ratios of (a) 1-sample A, (b) 2-sample B, (c) 3-sample C, and (d) 5sample D, at a rate of 0.24 Å/s. All AFM scans are $2 \times 2 \mu m^2$. Each inset shows the corresponding RHEED pattern along the $[11\overline{2}]$ direction taken immediately after growth.

surface morphologies of Samples A, B and C, it is clear that the film coalescence improves as the Te/Sn flux ratio increases from 1 to 3. The rough surface observed in Samples A and B may be caused by the high desorption rate of tellurium. It was determined previously, that the desorption rate of tellurium exceeds 0.8 Å/s at this substrate temperature (340 °C). 48,49 Tellurium desorption may lead to a tin-rich growth front, resulting in randomly shaped SnTe nuclei rather than lateral film coalescence with atomic triangular terraces observed in Figure 2c. The AFM image for Sample C (Figure 2c) with a 3:1 Te/Sn flux ratio shows a coalesced SnTe film without any granular features; its RMS roughness of 0.91 nm is the lowest in this series of samples. However, small triangular voids are still observed in Sample C. The area density of these voids (determined by measuring the number of voids in a larger 10 × 10 μ m² AFM image shown in Figure S2), is ~3 × 10⁹ cm⁻². In an attempt to reduce the density of voids, the Te/Sn flux ratio was further increased to 5 in Sample D. Unfortunately, this resulted in the surface becoming granular again, with reduced coalescence and an increased RMS roughness (Figure 2d). The increased roughness and incomplete coalescence may be attributed to a severely reduced tin adatom diffusion length due to the oversupply of tellurium, resulting in island formation instead of a coalesced layer. In summary, a Te/Sn flux ratio of 3 yields a coalesced SnTe film with an RMS roughness less than 1 nm.

4.1. Effect of Growth Rate on Film Surface Morphology and Crystallinity. The effect of growth rate on the quality of the SnTe thin film was studied next. The substrate temperature was kept at 340 °C, the Te/Sn flux ratio at ~3, and the film thickness at 15 nm for Sample E (grown at a rate of 0.06 Å/s), Sample F (grown at a rate of 0.12 Å/s), and Sample G (grown at a rate of 0.48 Å/s). These samples are directly compared to Sample C (discussed in the previous section and grown at a rate of 0.24 Å/s). All growth conditions for this series of samples are listed in detail in Table 2. Figure 3

Table 2. Summary of the Growth Parameters of Samples E to G; Sn Flux, Te Flux, Te/Sn Flux Ratio, and Film Growth Rate^a

sample no.	Sn flux (cm ⁻² /s)	Te flux (cm ⁻² /s)	Te/Sn flux ratio	SnTe growth rate (Å/s)	RMS roughness (nm)
Е	9.5×10^{12}	2.9×10^{13}	3	0.06	no film growth
F	1.9×10^{13}	5.8×10^{13}	3	0.12	5.6
C	3.8×10^{13}	1.1×10^{14}	3	0.24	0.9
G	7.6×10^{13}	2.3×10^{14}	3	0.48	0.2

 $^a{\rm The}$ RMS film surface roughness measured from a 2 \times 2 $\mu{\rm m}^2$ AFM image for each sample is also listed.

shows AFM images of the films along with the corresponding RHEED patterns for the four samples. For comparison purposes, Figure 2c for Sample C is presented again as Figure 3c. During the growth of Sample E with the lowest growth rte, the in situ RHEED pattern remained largely unchanged from the typical InP RHEED patterns, indicating no SnTe crystallites nucleated. Figure 3a therefore shows the bare InP substrate with no SnTe film. The lack of a film is likely due to a combination of the nonzero re-evaporation of SnTe at 340 °C and the slow growth rate. If the rate of arriving Sn adatoms is lower than the re-evaporation rate, no nuclei will be able to form. A growth rate of 0.12 Å/s (Sample F) results in a rough

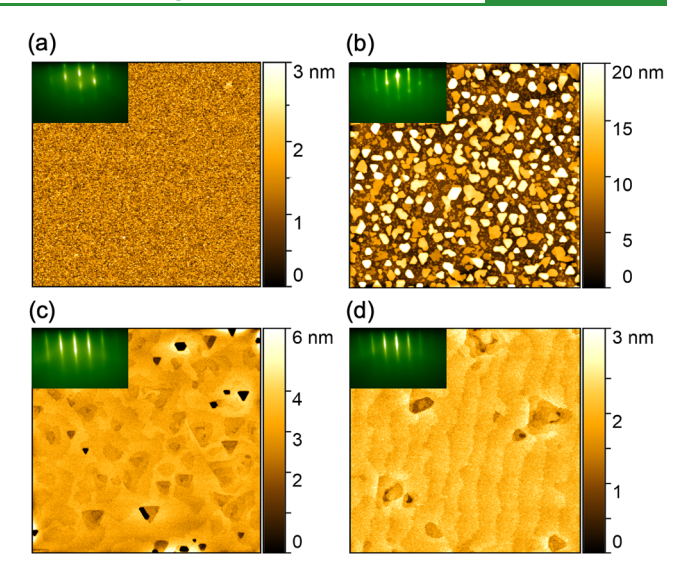


Figure 3. 2 × 2 μ m² AFM scans of Sample E (a), F (b), C (c), and G (d), grown at a rate of 0.06, 0.12, 0.24, 0.48 Å/s, respectively. Panel (c) is the same as Figure 2c. Each inset shows the corresponding RHEED pattern along the [11 $\overline{2}$] direction taken immediately after growth.

surface with SnTe nano-island formation, as shown in Figure 3b. Compared to Sample C, the surface in Sample F is not coalesced, and the orientations of SnTe nano islands are also random and not aligned. This indicates that the SnTe film does not easily wet the substrate, and reducing the film growth does not favor the surface morphology of the SnTe film.

Contrary to the rough and uncoalesced surfaces obtained with a slow growth rate, a smooth SnTe film has been obtained with a fast growth rate of 0.48 Å/s (Sample G), as shown in Figure 3d. The SnTe film of Sample G is similar to Sample C but shows an even further reduced RMS roughness of 0.2 nm compared to Sample C (0.9 nm). In contrast to Sample C, where several triangular voids can be observed, the surface of Sample G is almost free of voids (as shown by the larger-area AFM image in Figure S2 in the Supporting Information) and shows clear step edges. The step height of ~0.6 nm between surface terraces is consistent with the lattice constant of SnTe. The presence of atomic terraces free of bilayer nucleation sites indicates a step flow growth mode for the SnTe film. The density of the triangular voids in Sample C, as measured by the number of voids over the entire area in Figure S1, is $\sim 3 \times 10^9$ cm⁻²; the void density is reduced by 3 orders of magnitude to 5×10^6 cm⁻² for Sample G. The improvement in surface morphology with increasing growth rate is somewhat counterintuitive but can be explained by realizing that the higher growth rate suppresses the diffusion of metal (Sn) atoms and limits 3D island formation. Similar phenomena are observed in III–V semiconductors such as InAs.⁵⁰ In addition, a substrate temperature of 340 °C is quite close to the complete thermal decomposition point of 350 °C. At this temperature, therefore, we expect significant film re-evaporation (again, this is why no SnTe film was observed for sample E—the re-evaporation rate was higher than the deposition rate). For cubic materials grown along the (111) direction, film re-evaporation typically results in triangular pits, similar to those shown in Figure 3c. When the tin flux is increased, the film growth rate increases relative to the film re-evaporation rate, therefore suppressing the formation of triangular voids. It is expected that further increasing the growth rate would lead to further improvements

in surface morphology. However, the maximum growth rate in this study was kept at 0.48 Å/s (Sample G) due to the physical limitations of effusion cell operations for both elements Sn and

Figure 4 shows the XRD 2θ – ω scans for Samples F, C, and G, respectively (sample E is not shown as no film formed).

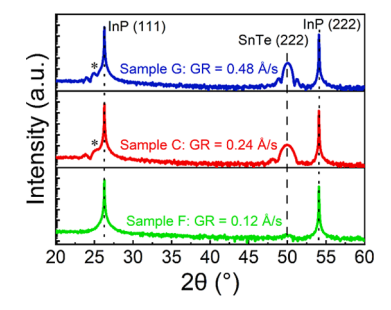


Figure 4. XRD $2\theta-\omega$ scans for Samples F—green, C—red, and G blue grown at a growth rate of 0.12, 0.24, and 0.48 Å/s, respectively. The vertical short-dashed lines highlight the InP (111) and (222) substrate diffraction peaks and the vertical long-dashed line indicates the position of the SnTe (222) peaks. The peak or bump marked by "*" denotes the approximate position of the SnTe (111) peaks.

Single phase SnTe (111) films were observed for all three samples, evidenced by the strong SnTe (222) diffraction peak at $\sim 50^{\circ}$. An additional peak at $\sim 25^{\circ}$ could be observed in both Samples C and G, which was identified as the SnTe (111) diffraction peak. The exact position of the SnTe (111) diffraction peak was, however, impossible to extract due to its vicinity to the InP (111) substrate diffraction peak 26°. Nonetheless, by applying Bragg's Law using the (222) peak,⁵¹ the out-of-plane lattice constant a₀ of cubic SnTe was calculated to 6.31 Å, which is in good agreement with previously reported values. 32,33,52 It is worth noting that interference fringes due to Pendellösung oscillations can be clearly observed surrounding both the SnTe (111) and (222) diffraction peaks in Sample G, indicative of an abrupt and sharp interface between the SnTe film and the InP substrate, in addition to the atomically flat SnTe film surface.⁵³ It is thus evident that a high growth rate leads to a flatter SnTe layer and benefits greatly its long-range crystallographic order.

4.2. Optimized SnTe Thin Films and Their Structural Properties. High resolution XRD scans were performed to investigate the crystalline quality of Sample G-grown under optimized conditions as determined above (340 °C, Te/Sn flux ratio of 3, and growth rate of 0.48 Å/s)—in detail. Figure 5a,b show rocking curves around the SnTe (222) and (220) diffraction peaks. Both curves have a sharp and single-peak Gaussian-like distribution. By applying a Pseudo-Voigt fitting profile,⁵⁴ the fwhm extracted from the SnTe (222) rocking curve is 0.09°, while that of the SnTe (220) is 0.42°. The fwhm of the SnTe (222) rocking curve is the lowest reported so far with similar film thickness, while the fwhm of SnTe (220), an in-plane orientation, has not been previously reported. The low fwhm values in both rocking curves confirm the high crystalline quality of the 15 nm film. Furthermore, for a thicker film $(\sim 100 \text{ nm})$ grown with the same growth parameters, the fwhm of SnTe (222) and (220) rocking curves (not shown) have been reduced to 0.06 and 0.16° , respectively, indicating a further improved crystalline quality and annihilation of threading dislocations as the film thickness increases. It is

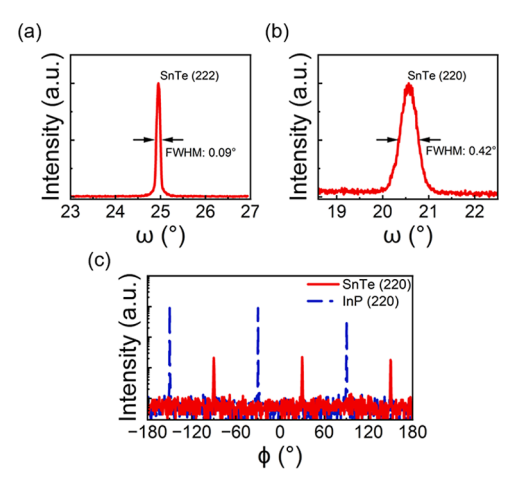


Figure 5. XRD rocking curves of SnTe along the (a) (222) and (b) (220) directions. (c) In-plane ϕ -scan of the SnTe (220) diffraction peak. The ϕ -scan for the InP substrate (220) diffraction peak is presented in the blue dashed line for reference.

expected that both XRD rocking curve fwhm can be further reduced by simply increasing the SnTe film thickness.

Finally, the XRD in-plane ϕ -scan around the SnTe 220 reflection is shown in Figure 5c. An in-plane rotational ϕ -scan is an effective method for measuring the density of rotational twin domains in the film. 55 The ϕ -scan for InP along the 220 reflection is presented as a reference. For the InP scan (shown in the blue dashed line), three peaks can be observed, corresponding to the 3-fold in-plane rotational symmetry of the (111)-oriented substrate. For the SnTe film, mimicking the InP substrate, an identical set of only three peaks separated by 120° is observed, indicating that the film is free of twin defects which act as scattering centers in electronic devices and nonradiative recombination pathways in optical devices. It is also noted that a 60° phase difference is observed between SnTe and InP substrate, suggesting an in-plane domain rotation. This is commonly observed in III-V epitaxial layers as well as other chalcogenide epitaxial layers, 44,56 and indicates the presence of in-plane misfit dislocations. In the past, twin defects have been observed in SnTe films grown on CdTe (111) buffer layers,⁵⁷ which was attributed to the presence of domains with different stacking orders.⁵⁸ In the current study, such twin domains have been eliminated, further confirming the excellent crystallinity in the as-grown optimized SnTe films.

To evaluate the strain state and degree of relaxation of optimized SnTe films, i.e., Sample G, RSM was conducted. Figure 6a and b show the RSM spectra around the symmetrical [222] and asymmetrical [224] directions. Both reciprocal space maps depict two clear peaks, one corresponding to the InP substrate and one corresponding to the SnTe film. The well-defined centers in the mosaic spread of both the SnTe (222) and SnTe (224) spots suggest that the as-grown SnTe epilayer has a high degree of crystalline alignment and structural coherence. In Figure 6a, the Bragg peaks of SnTe (222) and InP (222) are both on the $Q_x = 0$ line, confirming that the SnTe (111) planes are fully aligned with the InP substrate with no miscut or tilt. In Figure 6b, the relaxation of the SnTe film relative to the InP substrate is investigated. In a fully relaxed cubic structure, a theoretical angle of 19.471° is expected between the [111] and [224]. The angle between the mosaic center of the InP (224) reflection and the [111]

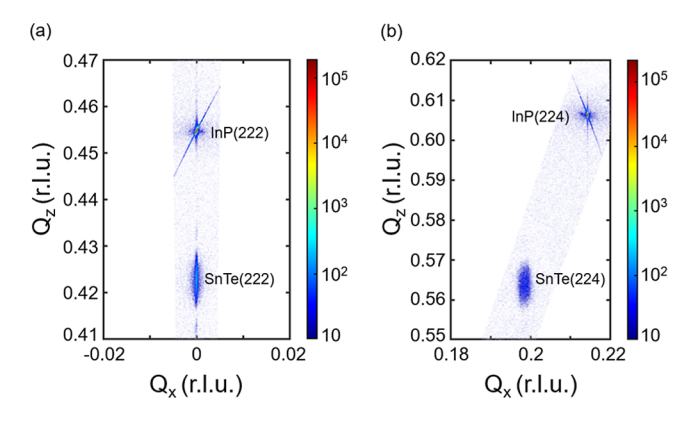


Figure 6. Reciprocal space maps of XRD peaks around the (a) InP (222) and (b) InP (224) diffractions. Both SnTe (222) and SnTe (224) mosaics are clearly observed and labeled in both figures, respectively.

direction was calculated to be 19.466° from the RSM in Figure 6b, which agrees well with the theoretical value. A similar good agreement to the theoretical value was calculated from the RSM for the angle between the SnTe (224) mosaic center and the [111] direction of 19.461°, suggesting the current 15 nm epitaxial SnTe film is already fully relaxed despite the >7% lattice mismatch between film and substrate.

Considering the relatively low dislocation density in the asgrown SnTe layer as evidenced from the narrow XRD rocking curves, one would expect a SnTe layer of ~15 nm to be partially strained to the substrate, since the critical thickness of SnTe on InP is ~4.5 nm. However, as discussed above, RSM indicates that the present 15 nm-thick SnTe film is fully relaxed. To elucidate the relaxation mechanism, STEM imaging at the SnTe/InP interface was performed. HAADF–STEM image of the SnTe/InP heterointerface along the [110] zone axis is shown in Figure 7a. A highly crystalline SnTe layer can be observed with the β -polytype, with brighter contrast as compared to the InP substrate region. A hazy atomically thin region presents at the SnTe/InP heterointerface, which generally indicates the presence of dislocations. ³⁹ To clarify

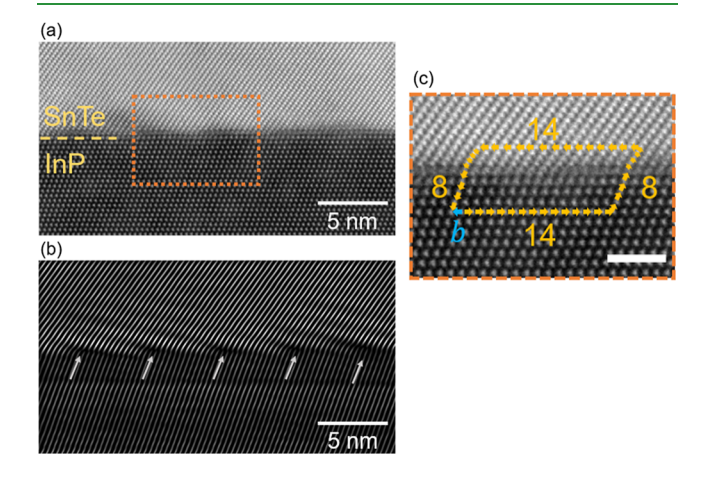


Figure 7. (a) HAADF–STEM image of SnTe film on InP (111)A. The dashed line indicates the interface between the SnTe film and the InP substrate. (b) Inverse FFT analysis of (a) using the [-111] spot. Each arrow highlights an IMF dislocation at the heterointerface. (c) A constructed Burgers circuit in the boxed region (marked in orange) of (a). The resulting Burgers vector is denoted in blue. The scale bar is 2 nm.

the positions and spacing between these dislocations, fast Fourier transform (FFT) analysis was performed using the image in Figure 7a. After using a masking filter of the FFT image around the [-111] spots, we then perform the inverse FFT analysis, following the technique of ref 44 which is shown in Figure 7b. This analysis clearly highlights the IMF dislocations that are uniformly spaced. The spacing between each misfit dislocation is ~ 5.2 nm, which corresponds to 13 SnTe lattice sites and 14 InP lattice sites. This distinguishes these results from the previous report of PbTe (111) layer on InP (111)A substrate, where misfit dislocations at the interface are mostly random and of various types. Conversely, the misfit dislocations shown in Figure 7a are highly periodic across the entire sample, characteristic of the formation of an IMF array. Here we have the sample of the formation of an IMF array.

To further explore the origin of the misfit dislocations, a right-hand Burger's circuit was constructed starting in the InP substrate, as demonstrated in Figure 7c. This resulted in a Burgers vector (b) with a length of 1 InP lattice site that lies completely in the plane of the SnTe/InP (111) heterointerface, which indicates that the Burgers vector is of the $\frac{a}{2}\langle 110\rangle$ type, i.e., a 60° misfit dislocation. 44 In III/V on III/V heteroepitaxy (e.g., GaSb on GaAs), IMF arrays have been previously observed to serve as the main mechanism for rapid strain relaxation. 40,41,43,44 Unlike previous observations, this work demonstrates an IMF array in a system with heterogeneous crystal structures, i.e., rock-salt epitaxial layer on a zinc-blende substrate, and furthermore in a system with differing cations and anions in the film and substrate, i.e. a IV-VI semiconductor film grown on a III-V substrate. Finally, the IMF array was observed for a film and substrate in the (111)orientation, which was only recently demonstrated in III-V heteroepitaxy.44

5. CONCLUSION

In summary, this work presents detailed investigations of MBE-grown SnTe epitaxial layers and discusses how the growth conditions impact surface morphology and crystalline quality. An increase of substrate temperature from 200 to 300-340 °C results in a transition from polycrystalline to single crystalline SnTe formation. An optimized Te/Sn flux ratio is found to lead to atomically smooth SnTe layers with triangular void formation. As the growth rate of the SnTe film increases, the surface morphology is substantially improved, as the density of triangular voids is reduced by 3 orders of magnitude. With these optimized growth parameters, largearea and high-quality SnTe (111) layers with a RMS roughness as low as 0.2 nm and an XRD rocking curve fwhm as low as 0.09°, both of which are state-of-the-art values, is obtained. The film is free of rotational twin domains, and the strain is fully relaxed despite the >7% lattice mismatch between film and substrate. Surprisingly, this work uncovers that the strain is relieved through the formation of a periodic IMF array at the SnTe/InP heterointerface, where each misfit dislocation is evenly spaced at 13 SnTe and 14 InP lattice sites. This highly efficient IMF array relaxes the lattice strain rapidly and leads to the observed high quality of the SnTe film. This is the first demonstration of the formation of an IMF array in a rock-salt on zinc-blende material system, as well as the first instance of such between an IV-VI epitaxial layer on a III-V substrate. This result highlights that IMF arrays can be used to relax strain in a much wider range of heteroepitaxial systems than

previously realized. These important observations thus facilitate the heterointegration of an important IV–VI semiconductor on a III–V substrate, unlocking the potential of creating high performance multifunctional devices. The smooth, relaxed, single crystalline SnTe films could also be used for infrared detectors, infrared plasmonics, and as a model system to understand the behavior of topological crystalline insulators when integrated with an InP back gate.

ASSOCIATED CONTENT

Data Availability Statement

The data sets that support the findings of this study are openly available at https://doi.org/10.26207/k2f9-ry44.

5 Supporting Information

The Supporting Information is available free of charge at https://pubs.acs.org/doi/10.1021/acsami.4c10296.

XRR data and fitting for the SnTe layer thickness of sample G; large-area AFM images of sample C and sample G (PDF)

AUTHOR INFORMATION

Corresponding Authors

Qihua Zhang — Two Dimensional Crystal Consortium Materials Innovation Platform, The Pennsylvania State University, University Park, Pennsylvania 16802, United States; orcid.org/0000-0002-7144-6988; Email: qzz5173@psu.edu

Stephanie Law — Two Dimensional Crystal Consortium Materials Innovation Platform, The Pennsylvania State University, University Park, Pennsylvania 16802, United States; Materials Research Institute, Department of Materials Science and Engineering, and Institute of Energy and the Environment, The Pennsylvania State University, University Park, Pennsylvania 16802, United States; ⊚ orcid.org/0000-0002-5087-6663; Email: sal6149@psu.edu

Authors

Maria Hilse – Two Dimensional Crystal Consortium Materials Innovation Platform, The Pennsylvania State University, University Park, Pennsylvania 16802, United States; Materials Research Institute and Department of Materials Science and Engineering, The Pennsylvania State University, University Park, Pennsylvania 16802, United States

Wesley Auker – Materials Research Institute, The Pennsylvania State University, University Park, Pennsylvania 16802, United States

Jennifer Gray — Materials Research Institute, The Pennsylvania State University, University Park, Pennsylvania 16802, United States

Complete contact information is available at: https://pubs.acs.org/10.1021/acsami.4c10296

Notes

The authors declare no competing financial interest.

ACKNOWLEDGMENTS

This research was conducted at the Pennsylvania State University Two-Dimensional Crystal Consortium—Materials Innovation Platform which is supported by NSF cooperative agreement DMR-2039351. The authors appreciate the use of the Penn State Materials Characterization Lab.

REFERENCES

- (1) Kihoi, S. K.; Shenoy, U. S.; Kahiu, J. N.; Kim, H.; Bhat, D. K.; Lee, H. S. Ultralow Lattice Thermal Conductivity and Enhanced Mechanical Properties of Cu and Sb Co-Doped SnTe Thermoelectric Material with a Complex Microstructure Evolution. *ACS Sustain. Chem. Eng.* **2022**, *10* (4), 1367–1372.
- (2) Chen, Z.; Guo, X.; Zhang, F.; Shi, Q.; Tang, M.; Ang, R. Routes for advancing SnTe thermoelectrics. *J. Mater. Chem. A* **2020**, 8 (33), 16790–16813.
- (3) Moshwan, R.; Yang, L.; Zou, J.; Chen, Z.-G. Eco-Friendly SnTe Thermoelectric Materials: Progress and Future Challenges. *Adv. Funct. Mater.* **2017**, *27* (43), 1703278.
- (4) Tan, G.; Shi, F.; Hao, S.; Chi, H.; Zhao, L.-D.; Uher, C.; Wolverton, C.; Dravid, V. P.; Kanatzidis, M. G. Codoping in SnTe: Enhancement of Thermoelectric Performance through Synergy of Resonance Levels and Band Convergence. *J. Am. Chem. Soc.* **2015**, 137 (15), 5100–5112.
- (5) Tan, G.; Zhao, L.-D.; Shi, F.; Doak, J. W.; Lo, S.-H.; Sun, H.; Wolverton, C.; Dravid, V. P.; Uher, C.; Kanatzidis, M. G. High Thermoelectric Performance of p-Type SnTe via a Synergistic Band Engineering and Nanostructuring Approach. *J. Am. Chem. Soc.* **2014**, 136 (19), 7006–7017.
- (6) Banik, A.; Biswas, K. Lead-free thermoelectrics: promising thermoelectric performance in p-type SnTe1-xSex system. *J. Mater. Chem. A* **2014**, 2 (25), 9620–9625.
- (7) Hwang, J.; Kim, H.; Han, M.-K.; Hong, J.; Shim, J.-H.; Tak, J.-Y.; Lim, Y. S.; Jin, Y.; Kim, J.; Park, H.; Lee, D.-K.; Bahk, J.-H.; Kim, S.-J.; Kim, W. Gigantic Phonon-Scattering Cross Section To Enhance Thermoelectric Performance in Bulk Crystals. ACS Nano 2019, 13 (7), 8347–8355.
- (8) Fu, L. Topological Crystalline Insulators. Phys. Rev. Lett. 2011, 106 (10), 106802.
- (9) Tanaka, Y.; Ren, Z.; Sato, T.; Nakayama, K.; Souma, S.; Takahashi, T.; Segawa, K.; Ando, Y. Experimental realization of a topological crystalline insulator in SnTe. *Nat. Phys.* **2012**, *8* (11), 800–803.
- (10) Hsieh, T. H.; Lin, H.; Liu, J.; Duan, W.; Bansil, A.; Fu, L. Topological crystalline insulators in the SnTe material class. *Nat. Commun.* **2012**, 3 (1), 982.
- (11) Zhang, D.; Baek, H.; Ha, J.; Zhang, T.; Wyrick, J.; Davydov, A. V.; Kuk, Y.; Stroscio, J. A. Quasiparticle scattering from topological crystalline insulator SnTe (001) surface states. *Phys. Rev. B: Condens. Matter Mater. Phys.* **2014**, 89 (24), 245445.
- (12) Akiyama, R.; Fujisawa, K.; Yamaguchi, T.; Ishikawa, R.; Kuroda, S. Two-dimensional quantum transport of multivalley (111) surface state in topological crystalline insulator SnTe thin films. *Nano Res.* **2016**, 9 (2), 490–498.
- (13) Zhang, Y.; Liu, Z.; Zhou, B.; Kim, Y.; Yang, L.; Ryu, H.; Hwang, C.; Chen, Y.; Hussain, Z.; Shen, Z.-X.; Mo, S.-K. ARPES study of the epitaxially grown topological crystalline insulator SnTe(111). *J. Electron Spectrosc. Relat. Phenom.* **2017**, 219, 35–40.
- (14) Klett, R.; Schönle, J.; Becker, A.; Dyck, D.; Borisov, K.; Rott, K.; Ramermann, D.; Büker, B.; Haskenhoff, J.; Krieft, J.; Hübner, T.; Reimer, O.; Shekhar, C.; Schmalhorst, J.-M.; Hütten, A.; Felser, C.; Wernsdorfer, W.; Reiss, G. Proximity-Induced Superconductivity and Quantum Interference in Topological Crystalline Insulator SnTe Thin-Film Devices. *Nano Lett.* **2018**, *18* (2), 1264–1268.
- (15) Iizumi, M.; Hamaguchi, Y.; Komatsubara, K.; Kato, Y. Phase Transition in SnTe with Low Carrier Concentration. *J. Phys. Soc. Jpn.* **1975**, 38 (2), 443–449.
- (16) Kobayashi, K. L. I.; Kato, Y.; Katayama, Y.; Komatsubara, K. F. Carrier-Concentration-Dependent Phase Transition in SnTe. *Phys. Rev. Lett.* **1976**, 37 (12), 772–774.
- (17) Sugai, S.; Murase, K.; Kawamura, H. Observation of soft TO-phonon in SnTe by Raman scattering. *Solid State Commun.* **1977**, 23 (2), 127–129.
- (18) Fei, R.; Kang, W.; Yang, L. Ferroelectricity and Phase Transitions in Monolayer Group-IV Monochalcogenides. *Phys. Rev. Lett.* **2016**, *117* (9), 097601.

- (19) Wan, W.; Liu, C.; Xiao, W.; Yao, Y. Promising ferroelectricity in 2D group IV tellurides: a first-principles study. *Appl. Phys. Lett.* **2017**, 111 (13), 132904.
- (20) Chang, K.; Liu, J.; Lin, H.; Wang, N.; Zhao, K.; Zhang, A.; Jin, F.; Zhong, Y.; Hu, X.; Duan, W.; Zhang, Q.; Fu, L.; Xue, Q.-K.; Chen, X.; Ji, S.-H. Discovery of robust in-plane ferroelectricity in atomic-thick SnTe. *Science* **2016**, 353 (6296), 274–278.
- (21) Huang, L.; Wu, F.; Li, J. Structural anisotropy results in straintunable electronic and optical properties in monolayer GeX and SnX (X = S, Se, Te). *J. Chem. Phys.* **2016**, *144* (11), 114708.
- (22) Liu, K.; Lu, J.; Picozzi, S.; Bellaiche, L.; Xiang, H. Intrinsic Origin of Enhancement of Ferroelectricity in SnTe Ultrathin Films. *Phys. Rev. Lett.* **2018**, *121* (2), 027601.
- (23) Yang, C.; Liu, Y.; Tang, G.; Wang, X.; Hong, J. Non-monotonic thickness dependence of Curie temperature and ferroelectricity in two-dimensional SnTe film. *Appl. Phys. Lett.* **2018**, *113* (8), 082905.
- (24) Song, W.; Cao, W.; Zhao, W.; Ding, J. Reproduced out-of-plane ferroelectricity in monolayer SnTe van der Waals heterostructures. *J. Phys.: Condens. Matter* **2023**, 35 (35), 355001.
- (25) Kim, J.; Kim, K.-W.; Shin, D.; Lee, S.-H.; Sinova, J.; Park, N.; Jin, H. Prediction of ferroelectricity-driven Berry curvature enabling charge- and spin-controllable photocurrent in tin telluride monolayers. *Nat. Commun.* **2019**, *10* (1), 3965.
- (26) Shin, D.; Sato, S. A.; Hübener, H.; De Giovannini, U.; Park, N.; Rubio, A. Dynamical amplification of electric polarization through nonlinear phononics in 2D SnTe. *npj Comput. Mater.* **2020**, *6* (1), 182
- (27) Weng, Z.; Ma, S.; Zhu, H.; Ye, Z.; Shu, T.; Zhou, J.; Wu, X.; Wu, H. CdTe thin film solar cells with a SnTe buffer layer in back contact. Sol. Energy Mater. Sol. Cells 2018, 179, 276–282.
- (28) Dey, M.; Dey, M.; Matin, M. A.; Amin, N. Design of high performance and ultra-thin CdTe solar cells with SnTe BSF from numerical analysis. In 2015 18th International Conference on Computer and Information Technology (ICCIT); IEEE, 2015; pp 573–576.
- (29) Antunez, P. D.; Buckley, J. J.; Brutchey, R. L. Tin and germanium monochalcogenide IV–VI semiconductor nanocrystals for use in solar cells. *Nanoscale* **2011**, 3 (6), 2399–2411.
- (30) Díaz, B.; Malachias, A.; Rappl, P. H. O.; Abramof, E.; Chitta, V. A.; Henriques, A. B. Growth of EuTe islands on SnTe by molecular beam epitaxy. *J. Cryst. Growth* **2010**, *312* (19), 2828–2833.
- (31) Díaz, B.; Malachias, A.; Montoro, L. A.; Rappl, P. H. O.; Abramof, E. Vertically ordered magnetic EuTe quantum dots stacks on SnTe matrices. *Nanotechnology* **2012**, *23* (1), 015604.
- (32) Yoshimi, R.; Masuko, M.; Ogawa, N.; Kawamura, M.; Tsukazaki, A.; Takahashi, K. S.; Kawasaki, M.; Tokura, Y. Versatile electronic states in epitaxial thin films of (Sn-Pb-In)Te: From topological crystalline insulator and polar semimetal to superconductor. *Phys. Rev. Mater.* **2021**, *5* (9), 094202.
- (33) Masuko, M.; Yoshimi, R.; Tsukazaki, A.; Kawamura, M.; Takahashi, K. S.; Kawasaki, M.; Tokura, Y. Molecular beam epitaxy of superconducting \${\mathrm{Sn}}_{1\text{\ensuremath{-}}x}-{\mathrm{In}}_{x}\mathrm{Te}\$ thin films. *Phys. Rev. Mater.* **2020**, *4* (9), 091202.
- (34) Su, N.; Tsuboi, K.; Kobayashi, S.; Sugimoto, K.; Kobayashi, M. Surface Morphology and Electronic Properties of SnTe Films Prepared by Molecular Beam Epitaxy. *Phys. Status Solidi* **2023**, 220 (8), 2200555.
- (35) Tsuboi, K.; Su, N.; Kobayashi, S.; Sugimoto, K.; Kobayashi, M. Molecular beam epitaxy of stoichiometric tin—telluride thin films. *J. Cryst. Growth* **2022**, 597, 126805.
- (36) Mengui, U. A.; Abramof, E.; Rappl, P. H. O.; Ueta, A. Y. Characterization of SnTe films grown by molecular beam epitaxy. *Braz. J. Phys.* **2006**, *36*, 324–327.
- (37) Yan, C.-H.; Guo, H.; Wen, J.; Zhang, Z.-D.; Wang, L.-L.; He, K.; Ma, X.-C.; Ji, S.-H.; Chen, X.; Xue, Q.-K. Growth of topological crystalline insulator SnTe thin films on Si(111) substrate by molecular beam epitaxy. *Surf. Sci.* **2014**, *621*, 104–108.

- (38) Babkevich, A. Y.; Cowley, R. A.; Mason, N. J.; Weller, S.; Stunault, A. X-ray scattering from dislocation arrays in GaSb. *J. Phys.: Condens. Matter* **2002**, *14* (49), 13505–13528.
- (39) Balakrishnan, G.; Huang, S.; Dawson, L. R.; Xin, Y. C.; Conlin, P.; Huffaker, D. L. Growth mechanisms of highly mismatched AlSb on a Si substrate. *Appl. Phys. Lett.* **2005**, *86* (3), 034105.
- (40) Huang, S. H.; Balakrishnan, G.; Khoshakhlagh, A.; Jallipalli, A.; Dawson, L. R.; Huffaker, D. L. Strain relief by periodic misfit arrays for low defect density GaSb on GaAs. *Appl. Phys. Lett.* **2006**, 88 (13), 131911.
- (41) Huang, S.; Balakrishnan, G.; Huffaker, D. L. Interfacial misfit array formation for GaSb growth on GaAs. *J. Appl. Phys.* **2009**, *105* (10), 103104.
- (42) Reyner, C. J.; Wang, J.; Nunna, K.; Lin, A.; Liang, B.; Goorsky, M. S.; Huffaker, D. L. Characterization of GaSb/GaAs interfacial misfit arrays using x-ray diffraction. *Appl. Phys. Lett.* **2011**, 99 (23), 231906.
- (43) Benyahia, D.; Kubiszyn, Ł.; Michalczewski, K.; Kębłowski, A.; Martyniuk, P.; Piotrowski, J.; Rogalski, A. Interfacial Misfit Array Technique for GaSb Growth on GaAs (001) Substrate by Molecular Beam Epitaxy. *J. Electron. Mater.* **2018**, *47* (1), 299–304.
- (44) Nordstrom, M. D.; Garrett, T. A.; Reddy, P.; McElearney, J.; Rushing, J. R.; Vallejo, K. D.; Mukherjee, K.; Grossklaus, K. A.; Vandervelde, T. E.; Simmonds, P. J. Direct Integration of GaSb with GaAs(111)A Using Interfacial Misfit Arrays. *Cryst. Growth Des.* **2023**, 23 (12), 8670–8677.
- (45) Jung, J.; Schellingerhout, S. G.; van der Molen, O. A. H.; Peeters, W. H. J.; Verheijen, M. A.; Bakkers, E. P. A. M. Single-crystalline PbTe film growth through reorientation. *Phys. Rev. Mater.* **2023**, 7 (2), 023401.
- (46) Cheng, K. Y. Compound Semiconductor Crystals. In III-V Compound Semiconductors and Devices: An Introduction to Fundamentals; Cheng, K. Y., Ed.; Springer International Publishing, 2020; pp 105-159.
- (47) Horio, Y.; Yuhara, J.; Takakuwa, Y. Structural analysis of an InP(111)A surface using reflection high-energy electron diffraction rocking curves. *Jpn. J. Appl. Phys.* **2019**, 58 (SI), SIIA14.
- (48) Liu, D. S. H.; Hilse, M.; Engel-Herbert, R. Sticking coefficients of selenium and tellurium. *J. Vac. Sci. Technol.* **2021**, 39 (2), 023413.
- (49) Liu, D. S. H.; Hilse, M.; Engel-Herbert, R. Desorption characteristics of selenium and tellurium thin films. *J. Vac. Sci. Technol.* **2022**, *40* (5), 053407.
- (50) Law, S.; Yu, L.; Wasserman, D. Epitaxial growth of engineered metals for mid-infrared plasmonics. *J. Vac. Sci. Technol. B* **2013**, *31* (3), 03C121.
- (51) Fewster, P. F. X-Ray Scattering from Semiconductors; Imperial College Press And Distributed By World Scientific Publishing Co., 2003; p 316.
- (52) Kriener, M.; Kamitani, M.; Koretsune, T.; Arita, R.; Taguchi, Y.; Tokura, Y. Tailoring band structure and band filling in a simple cubic (IV, III)-VI superconductor. *Phys. Rev. Mater.* **2018**, *2* (4), 044802.
- (53) Batterman, B. W.; Hildebrandt, G. X-ray Pendellösung fringes in Darwin reflection. *Acta Crystallogr., Sect. A* **1968**, *24* (1), 150–157.
- (54) Langford, J. I.; Wilson, A. Scherrer after sixty years: a survey and some new results in the determination of crystallite size. *J. Appl. Crystallogr.* **1978**, *11* (2), 102–113.
- (55) Harrington, G. F.; Santiso, J. Back-to-Basics tutorial: X-ray diffraction of thin films. *J. Electroceram.* **2021**, 47 (4), 141–163.
- (56) Richardella, A.; Kandala, A.; Lee, J. S.; Samarth, N. Characterizing the structure of topological insulator thin films. *APL Mater.* **2015**, 3 (8), 083303.
- (57) Schreyeck, S.; Brunner, K.; Molenkamp, L. W.; Karczewski, G.; Schmitt, M.; Sessi, P.; Vogt, M.; Wilfert, S.; Odobesko, A. B.; Bode, M. Breaking crystalline symmetry of epitaxial SnTe films by strain. *Phys. Rev. Mater.* **2019**, *3* (2), 024203.
- (58) Chen, Y. P.; Faurie, J. P.; Sivananthan, S.; Hua, G. C.; Otsuka, N. Suppression of twin formation in CdTe(111)B epilayers grown by

molecular beam epitaxy on misoriented Si(001). J. Electron. Mater. 1995, 24 (5), 475-481.